Electronic Supplementary Material (ESI) for Journal of Materials Chemistry A.

Supporting Information

A universal route to N-coordinated metal anchored on porous carbon nanosheets for highly efficient oxygen electrochemistry

Jin-Tao Ren[a,b], and Zhong-Yong Yuan[a,b,*]

[a] National Institute for Advanced Materials, School of Materials Science and Engineering, Nankai University, Tianjin 300350, China.
[b] Key Laboratory of Advanced Energy Materials Chemistry (Ministry of Education), Collaborative Innovation Center of Chemical Science and Engineering (Tianjin), Nankai University, Tianjin 300071, China.
[*] Corresponding author. E-mail: zyyuan@nankai.edu.cn

1. Supplementary Figures

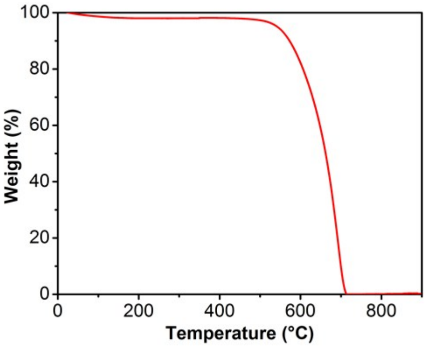

Fig. S1. Thermogravimetry analysis (TGA) curves of g-C_3N_4 in N_2 atmosphere. Obviously, the g-C_3N_4 decomposes completely at temperature above 710 ℃. Therefore, the use of g-C_3N_4 as template eliminates the requirement of post-synthetic removal of the template.

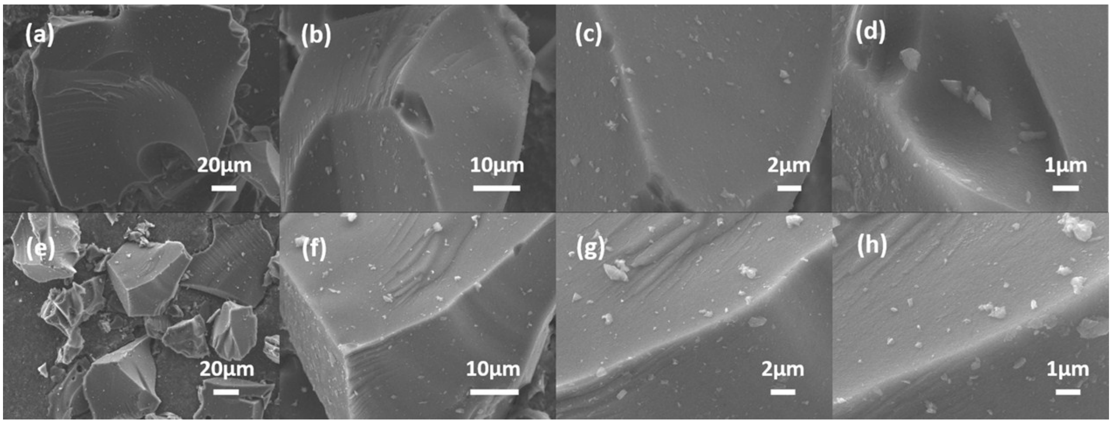

Fig. S2. SEM images of (a-d) Fe-N-C NC and (e-f) N-C NC. The Fe-N-C NC synthesized in the absence of g-C_3N_4 exhibits bulk morphology, which is evidently different to the porous sheets structure of Fe-N-C PCSs, indicating that the presence of g-C_3N_4 can evidently tailor the micro-structure of the resulting materials. In addition, the similar structure between Fe-N-C NC and N-C NC demonstrates that the addition of iron salts during the synthesis process has little effect on the final morphology.

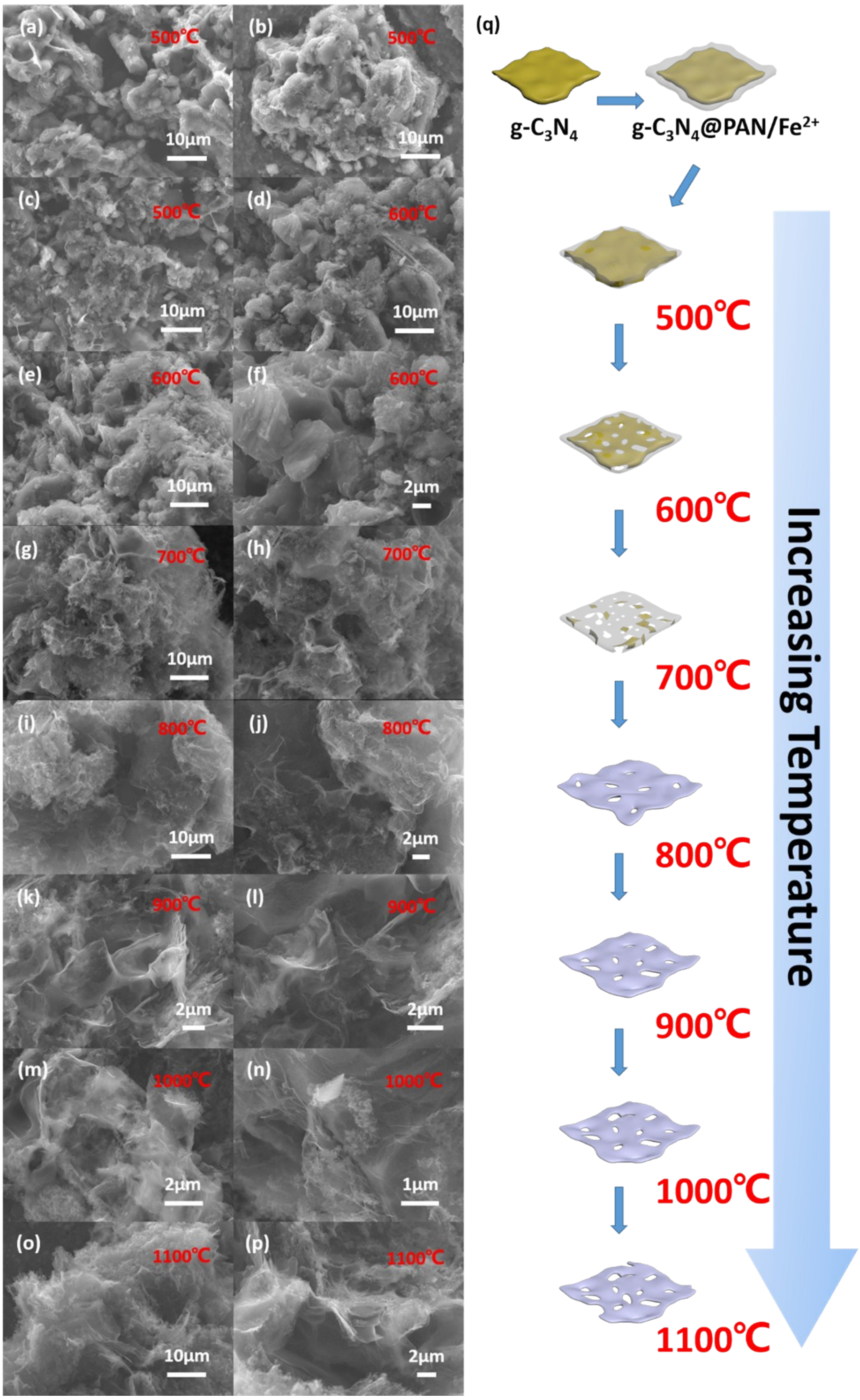

Fig. S3. SEM images of the series of Fe-N-C PCSs pyrolyzed at different annealing temperature, (a-c) 500 °C, (d-f) 600 °C, (g-h) 700 °C, (i-j) 800 °C, (k-l) 900 °C, (m-n) 1000 °C, (o-p) 1100 °C, (q) Schematic illustration of morphologies of samples obtained at different annealing temperature.

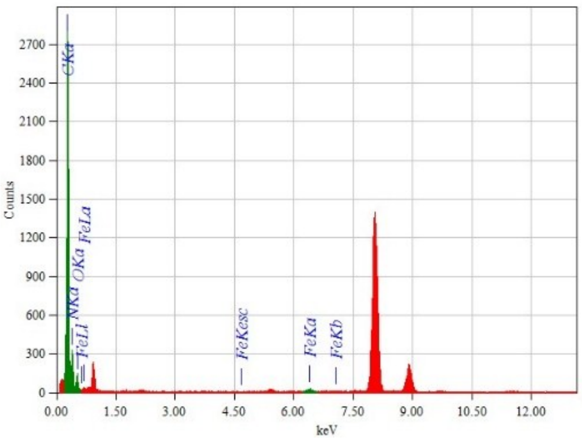

Fig. S4. TEM-EDX spectrum of Fe-N-C PCSs.

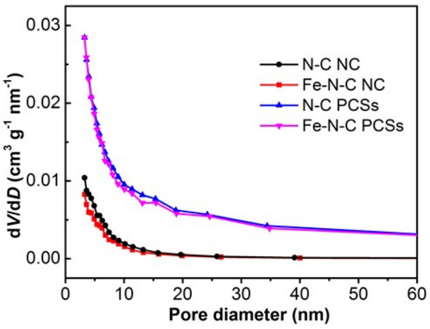

Fig. S5. Pore size distribution curves calculated from the adsorption branch of the isotherms of Fe-N-C PCSs, Fe-N-C NC, N-C PCSs, and N-C NC.

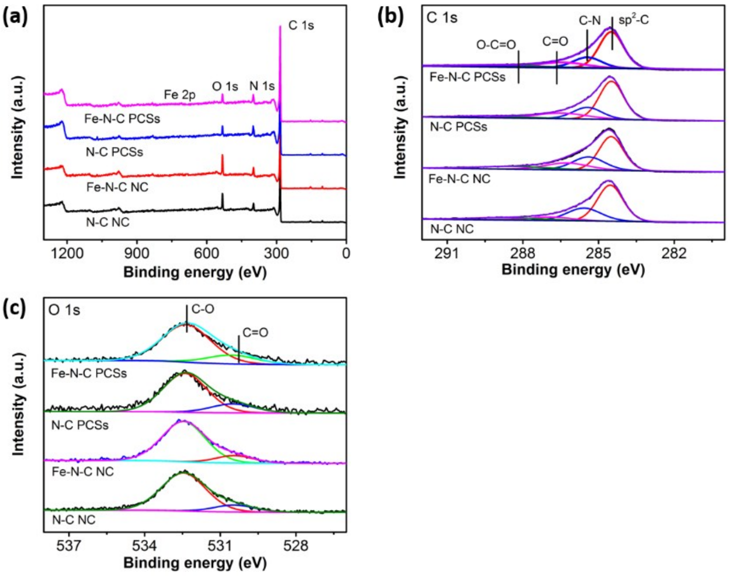

Fig. S6. (a) XPS survey, (b) C 1s, and (c) O 1s XPS spectra of Fe-N-C PCSs, Fe-N-C NC, N-C PCSs, and N-C NC.

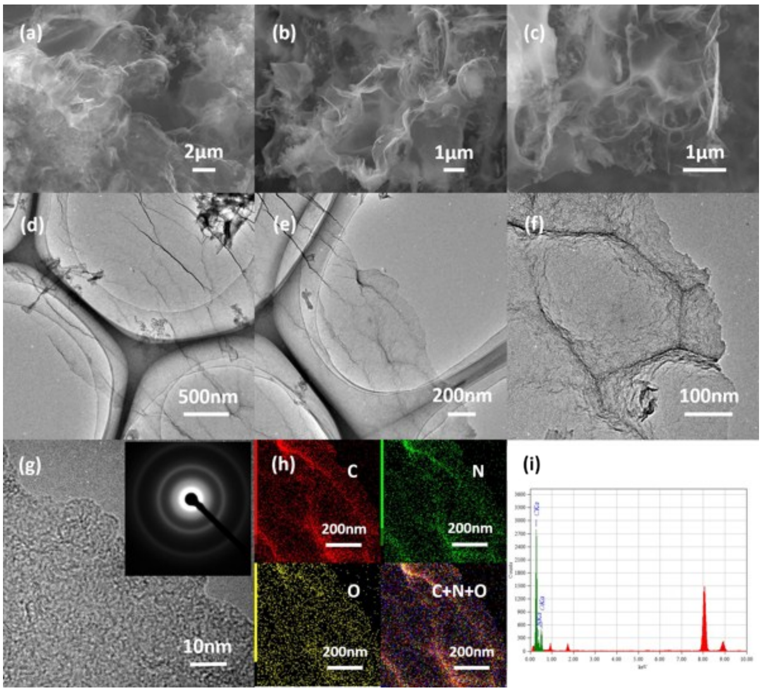

Fig. S7. (a-c) SEM, (d-f) TEM, (g) HR-TEM images of N-C PCSs. The inset of (g) shows the corresponding SAED pattern. (h) The corresponding TEM-EDX elemental mappings of N-C PCSs. (i) TEM-EDX spectrum of N-C PCSs.

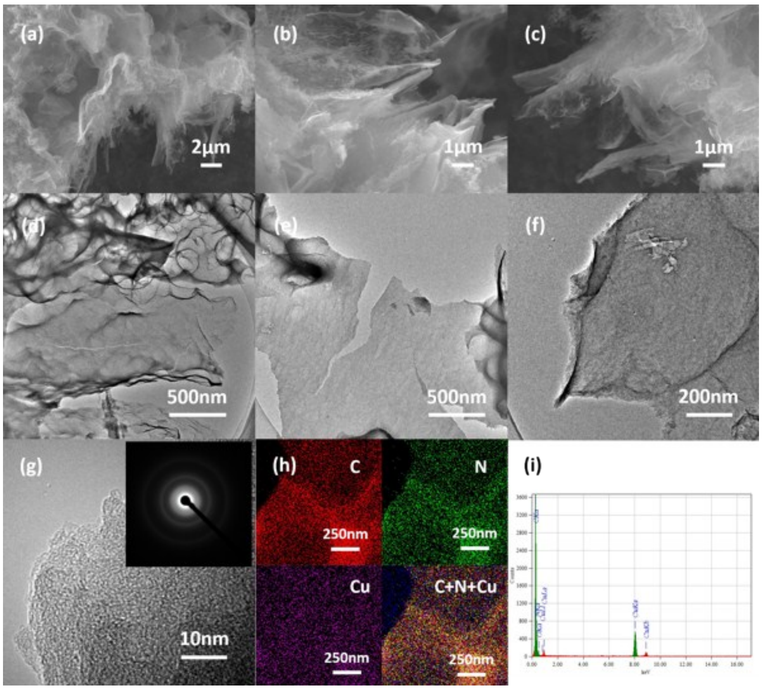

Fig. S8. (a-c) SEM, (d-f) TEM, (g) HR-TEM images of Cu-N-C PCSs. The inset of (g) shows the corresponding SAED pattern. (h) The corresponding TEM-EDX elemental mappings of Cu-N-C PCSs.

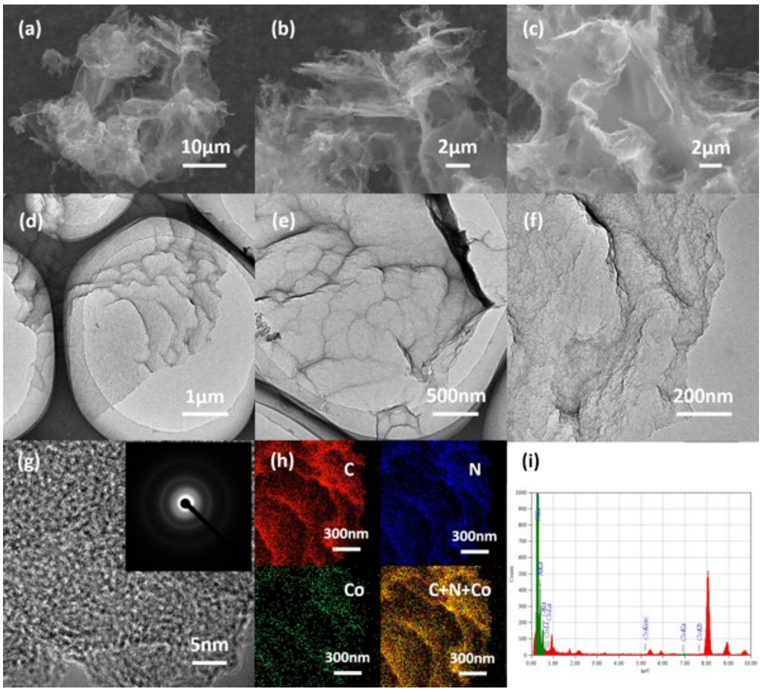

Fig. S9. (a-c) SEM, (d-f) TEM, (g) HR-TEM images of Co-N-C PCSs. The inset of (g) shows the corresponding SAED pattern. (h) The corresponding TEM-EDX elemental mappings of Co-N-C PCSs. (i) TEM-EDX spectrum of Co-N-C PCSs.

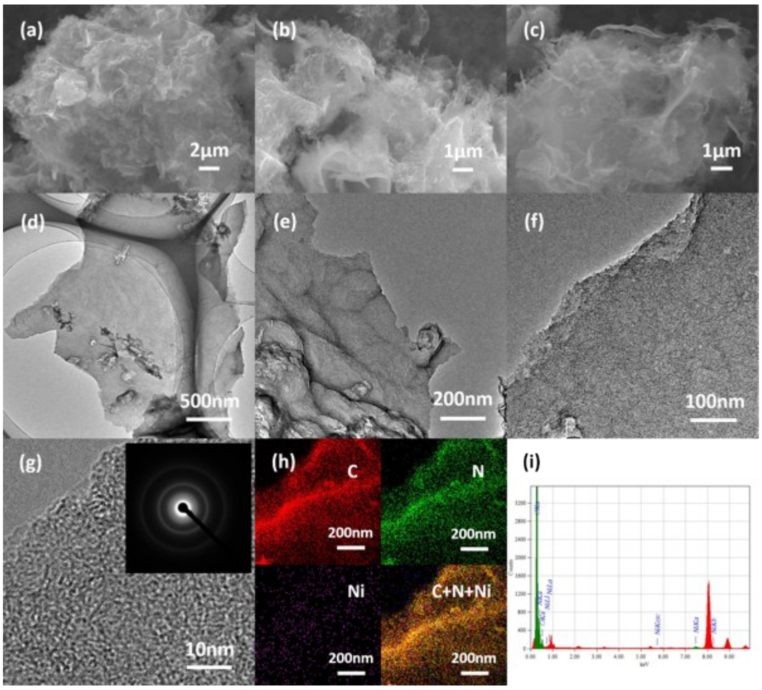

Fig. S10. (a-c) SEM, (d-f) TEM, (g) HAADF-STEM images of Fe-N-C PCSs. The inset of (f) shows the corresponding SAED pattern. (h) The corresponding TEM-EDX elemental mappings of Ni-N-C PCSs. (i) TEM-EDX spectrum of Ni-N-C PCSs.

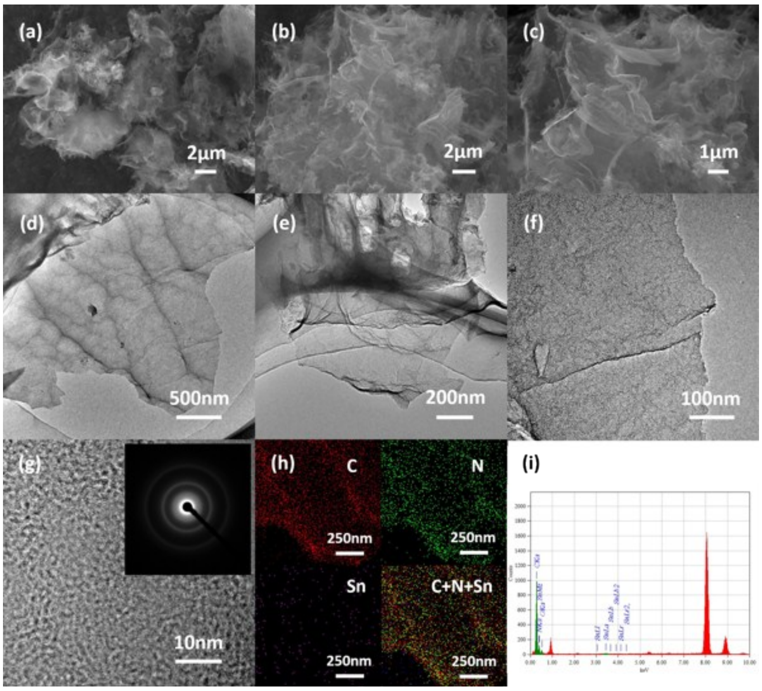

Fig. S11. (a-c) SEM, (d-f) TEM, (g) HAADF-STEM images of Fe-N-C PCSs. The inset of (f) shows the corresponding SAED pattern. (h) The corresponding TEM-EDX elemental mappings of Sn-N-C PCSs. (i) TEM-EDX spectrum of Sn-N-C PCSs.

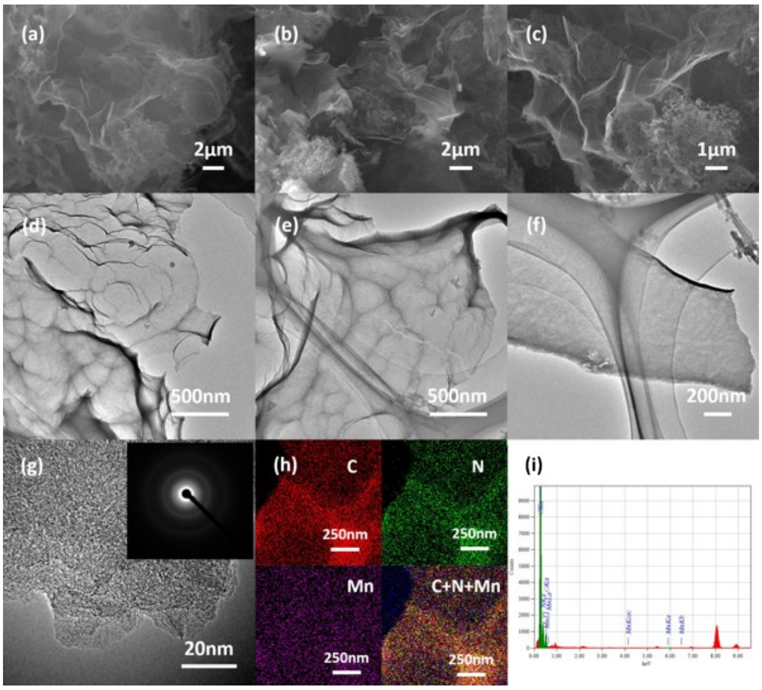

Fig. S12. (a-c) SEM, (d-f) TEM, (g) HAADF-STEM images of Fe-N-C PCSs. The inset of (f) shows the corresponding SAED pattern. (h) The corresponding TEM-EDX elemental mappings of Mn-N-C PCSs. (i) TEM-EDX spectrum of Mn-N-C PCSs.

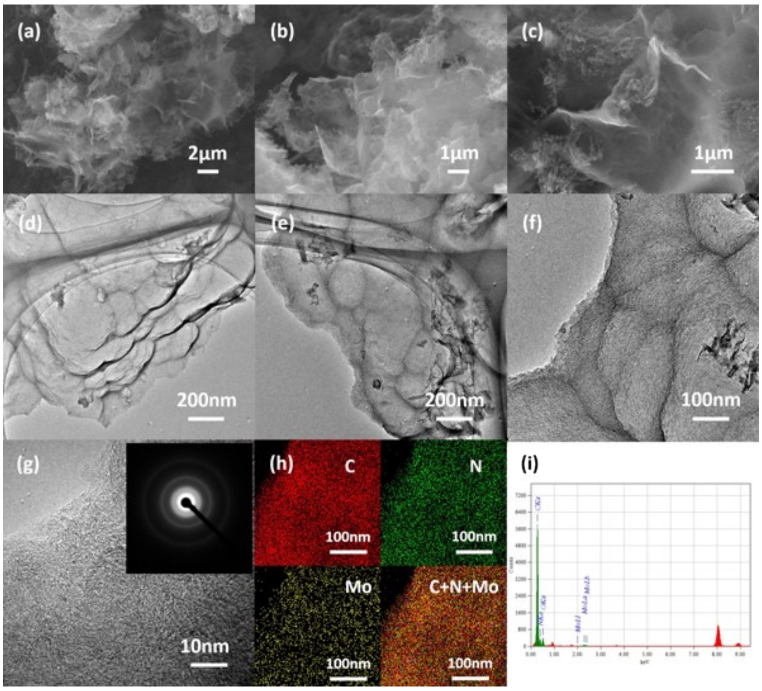

Fig. S13. (a-c) SEM, (d-f) TEM, (g) HR-TEM images of Mo-N-C PCSs. The inset of (f) shows the corresponding SAED pattern. (h) The corresponding TEM-EDX elemental mappings of Mo-N-C PCSs. (i) TEM-EDX spectrum of Mo-N-C PCSs.

For M-N-C PCSs, all the samples exhibit the sheet-like morphology with porous structure, and the metal species with low content are homogeneously dispersed on the carbon nanosheets without detected aggregation. The pyrolysis of the g-C_3N_4 template and further carbonization of the out polymer layers leads to the formation of porous carbon sheets.

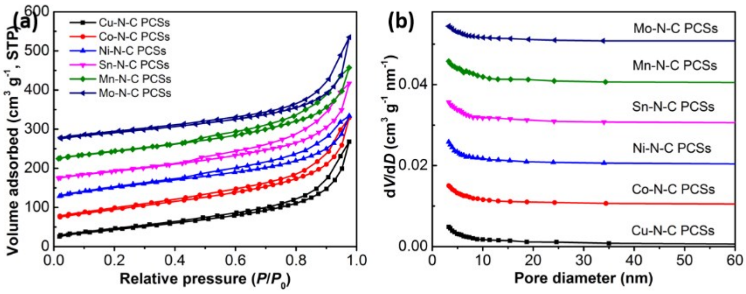

Fig. S14. (a) N_2 adsorption-desorption isotherms of the synthesized M-N-C PCSs, and their corresponding pore size distribution curves (b). The volume was shifted by 50, 100, 150, 200, and 250 and d*V*/d*D* value was shifted by 0.01, 0.02, 0.03, 0.04 and 0.05 for those curves, respectively. The BET specific surface area was determined to be 163, 175, 172, 161, 166, 152 m^2 g^{-1} for Cu/Co/Ni/Sn/Mn/Mo-N-C PCSs, associated with the total pore volume of 0.41, 0.43, 0.37, 0.41, 0.40, 0.44 m^3 g^{-1}, respectively.

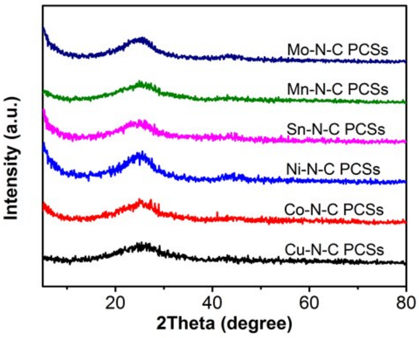

Fig. S15. XRD patterns of the prepared M-N-C PCSs. All the XRD patterns revealed the two graphtic-related peaks at approximate 25° and 44° (2θ), demonstrating the formation of graphitic carbon under high carbonization temperature.

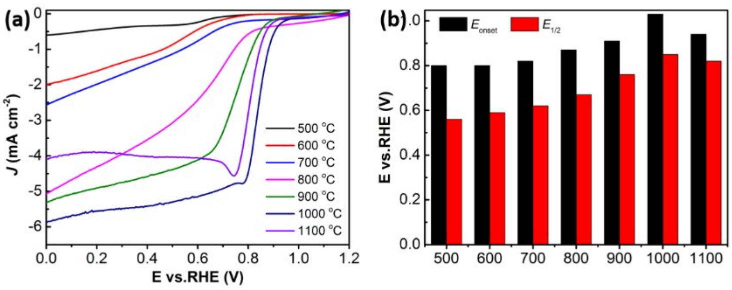

Fig. S16. (a) LSV polarization curves and (b) onset potentials and half-wave potentials of the series Fe-N-C PCSs catalysts obtained at different annealing temperature in O_2-saturated 0.1 M KOH solution. As shown in Fig. S16b, along with the pyrolysis temperature, the fabricated Fe-N-C PCSs exhibits an increased activity, as proved by their E_{onset} and $E_{1/2}$, indicating the carbonization temperature is a vital parameter to determine the electrocatalytic activity.

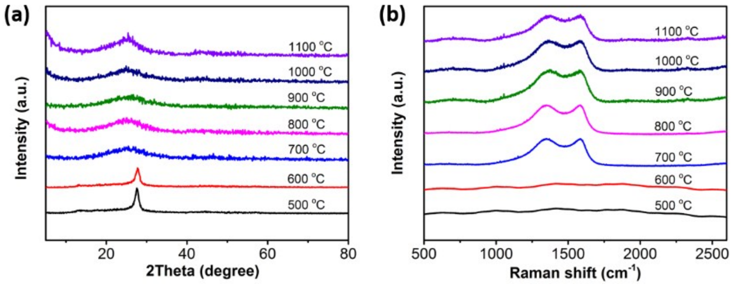

Fig. S17. (a) XRD patterns and (b) Raman spectra of the series of Fe-N-C PCSs catalysts prepared at different carbonization temperatures. The samples treated at 500 ℃ and 600 ℃ exhibit the typical XRD peaks for g-C_3N_4, while the XRD peaks related to graphitic carbon appear after the 700 ℃ treatment. And the peak intensity associated with graphitic carbon are gradually stronger, confirming the formation of graphitic structure. The Raman spectra of the series of Fe-N-C PCSs catalysts also show two peaks at 1350 and 1590 cm^{-1}, assigned to disordered sp^3 carbon (D band) and graphitic sp^2 carbon (G band), respectively, indicating the graphitic structure upon high temperature treatment.

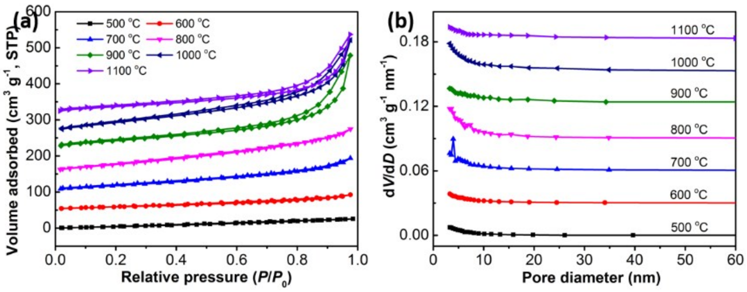

Fig. S18. N_2 adsorption-desorption isotherms of the Fe-N-C PCSs catalysts annealed at different temperatures. The volume was shifted by 50, 100, 150, 200, 250 and 300 and dV/dD value was shifted by 0.03, 0.06, 0.09, 0.12, 0.15 and 0.18 for those curves, respectively. The BET specific surface area (S_{BET}) was determined to be 29, 36, 74, 110, 151, 166, and 129 m^2 g^{-1} for the Fe-N-C PCSs catalysts obtained at different temperature. The incomplete pyrolysis at low temperature leads to the lower surface area, as proved by the gradually increased S_{BET} along with the increase of pyrolysis temperature. But the increased stacking degree would happened after further extending the calcination temperature, thus the lower S_{BET} was obtained by the samples treated at 1100 ℃.

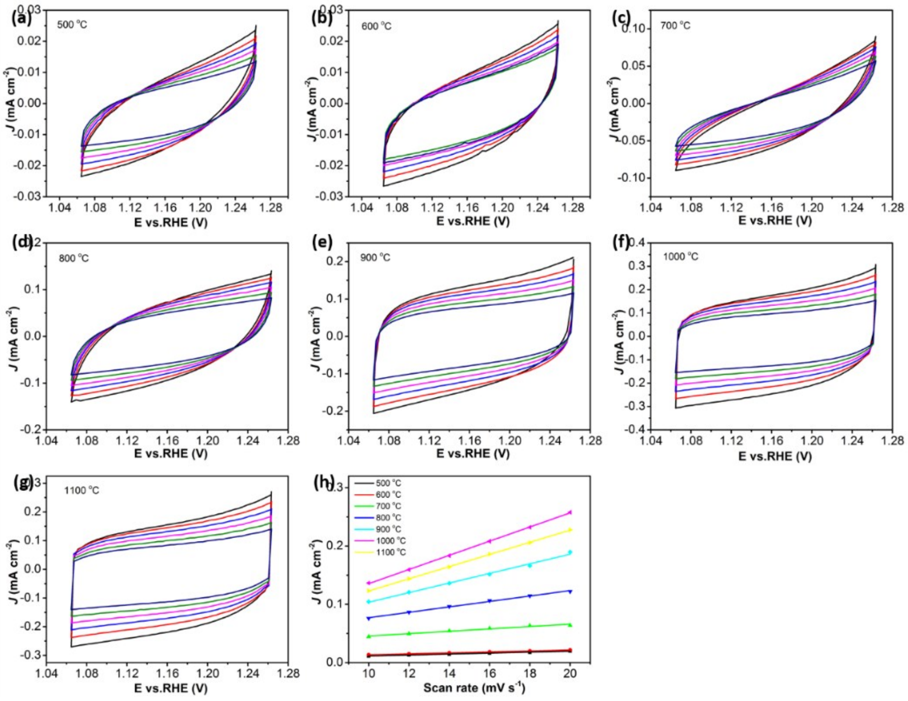

Fig. S19. (a) CV curves of the Fe-N-C PCSs catalysts annealed at different temperatures in N_2-saturated 0.1 M KOH solution. (e) Current densities at 1.24 V against the scan rates for the resulting catalysts. From the plots of current densities against scan rates, the electrochemical double-layer capacitance (C_{dl}) are determined to be 0.8, 0.8, 2.0, 4.7, 8.3, 12.2, and 10.4 mF cm^{-2}. It should be mentioned that the catalytic activity of electrocatalysts is considered to be related to the catalytically active surface area, namely, the C_{dl}. The much higher C_{dl} of the sample treated at 1000 ℃ indicated that the pyrolysis temperature at 1000 ℃ may be the optimal temperature for the develop of Fe-N-C PCSs.

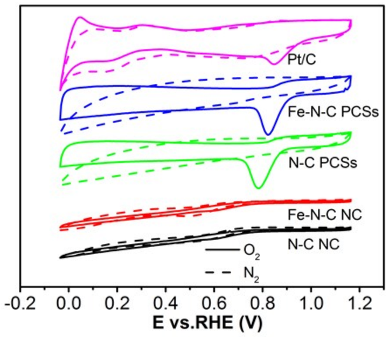

Fig. S20. Cyclic voltammograms (CVs) of commercial Pt/C, Fe-N-C PCSs, Fe-N-C NC, N-C PCSs, and N-C NC in N_2- and O_2-saturated 0.1 M KOH solution.

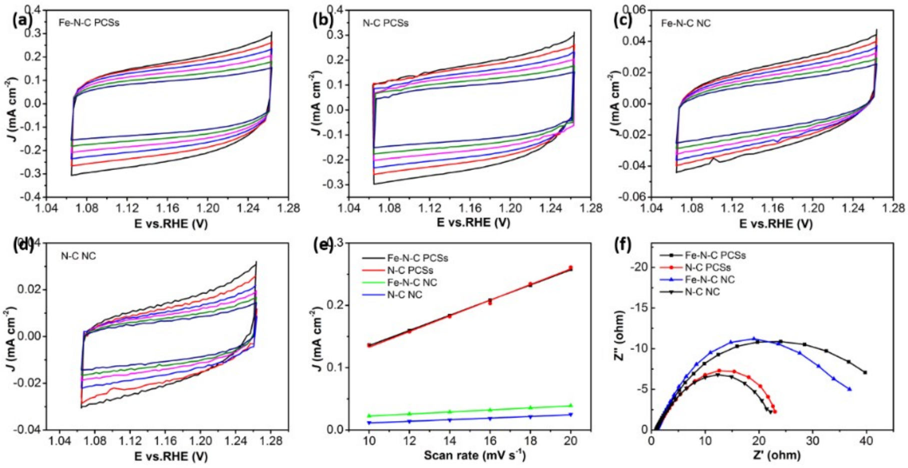

Fig. S21. CV curves of (a) Fe-N-C PCSs, (b) Fe-N-C NC, (c) N-C PCSs and (d) N-C NC in N_2-saturated 0.1 M KOH solution. (e) Current densities at 1.24 V against the scan rates for the resulting catalysts. (f) EIS plots of the Fe-N-C PCSs, Fe-N-C NC, N-C PCSs, and N-C NC, respectively. The electrochemical surface area (ECSA) and electrochemical impedance spectra (EIS), including Fe-N-C PCSs, Fe-N-C NC, N-C PCSs, and N-C NC, were measured to insight into the origin for the excellent ORR catalytic performance of Fe-N-C PCSs. It is considered that the double-layer capacitance (C_{dl}) of catalyst is linearly proportional to its electrochemical active surface area (ECSA), and the C_{dl} could be easily determined by their cyclic voltammetry (CV) measurements of different catalysts with different scan rates within a non-Faradic potential range in 0.1 M KOH solution. As shown in Fig. S21e, the Fe-N-C PCSs sample exhibits a C_{dl} of 12.2 mF cm^{-2}, which is much higher than that of Fe-N-C NC (1.7 mF cm^{-2}), N-C PCSs (12.0 mF cm^{-2}), and N-C NC (1.3 mF cm^{-2}). The higher C_{dl} value of Fe-N-C PCSs indicates the largest ECSA. In addition, the EIS measurements of these catalysts reveal that the Fe-N-C PCSs exhibit a smallest semicircle in their EIS plot, namely, the minimum charge transfer resistance (*R*ct), suggesting the fastest charge transfer ability from the porous carbon substrate to active sites, consequently, much favorable reaction kinetics. On the basis of the above results, it is noted that the ultrafine N-coordinated metal species and porous nanosheets structure together synergistically lead to the effective exposure of active sites and the enhanced electric conductivity, and thus resulting in the outstanding electrochemical reaction activities.

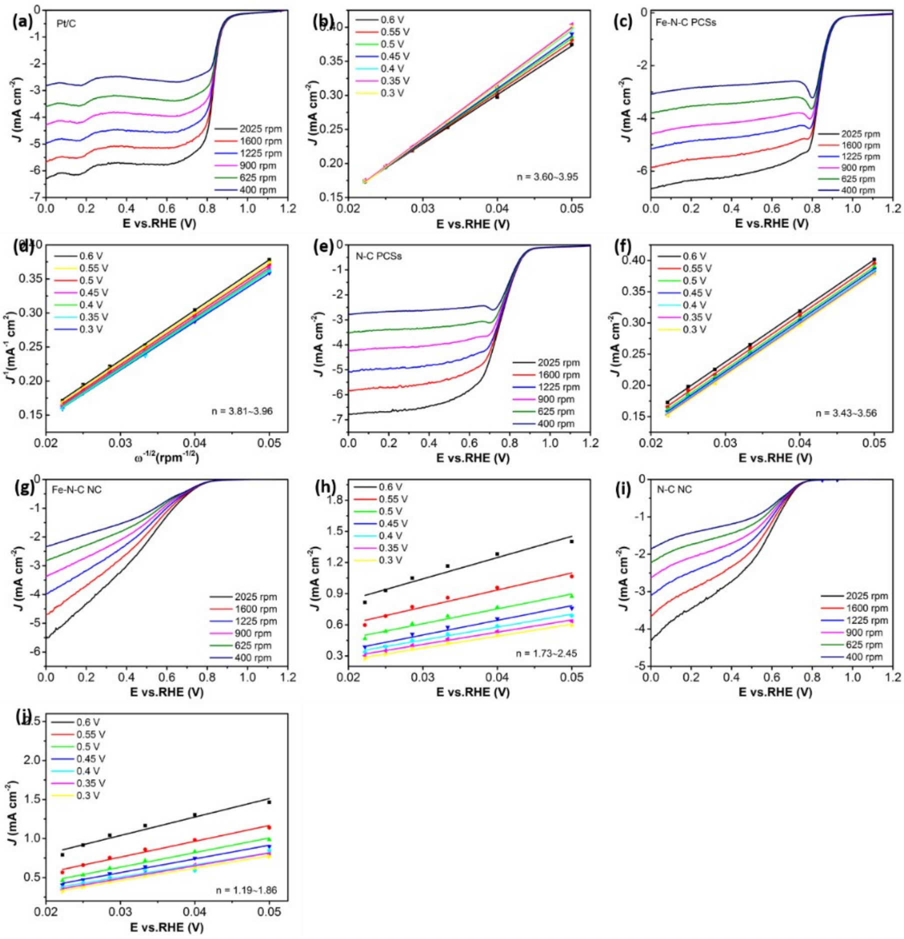

Fig. S22. ORR polarization curves of the developed catalysts under various rotating speeds and their corresponding K-L plots at 0.3-0.6 V. (a-b) commercial Pt/C catalyst; (c-d) Fe-N-C PCSs; (e-f) N-C PCSs; (g-h) Fe-N-C NC; (i-j) N-C NC. A series of more detailed investigation of RDE tests at different rotating speeds from 400 to 2025 rpm were examined to illustrate the electrochemical oxygen reduction mechanisms and the dominated processes. All of the catalysts reveal the increased current with the raise of rotating rate, as a result of the shortened diffusion distance at high speeds. The good linearity of the K-L plots exhibits the first-order reaction with respect to the concentration of dissolved oxygen. Form the slope of K-L plots, the electron transfer number (*n*) value per oxygen in the ORR process can be determined. As observed in Fig. S22, as compared with Fe-N-C NC, N-C PCSs, and N-C NC, Fe-N-C PCSs exhibit a higher n value of 3.81-3.96, close to those of commercial Pt/C catalyst, meaning that the perfect selectivity for the pseudo-four-electron dominated the ORR pathway.

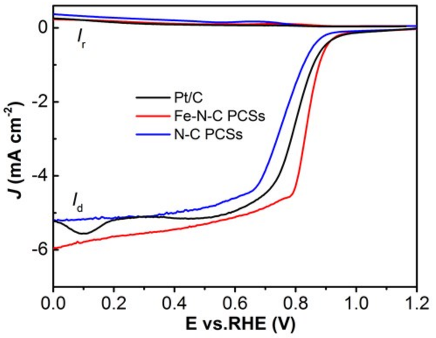

Fig. S23. The disk current (I_d) and ring current (I_r) of the prepared catalysts and commercial Pt/C catalysts in the RRDE test.

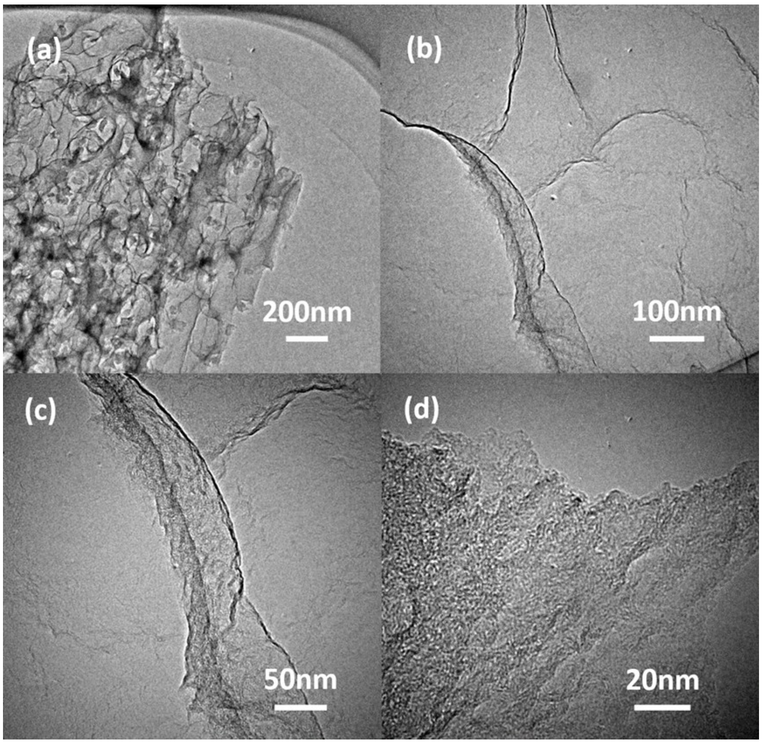

Fig. S24. (a-d) TEM images of Fe-N-C PCSs catalyst after 500 continuous cycles.

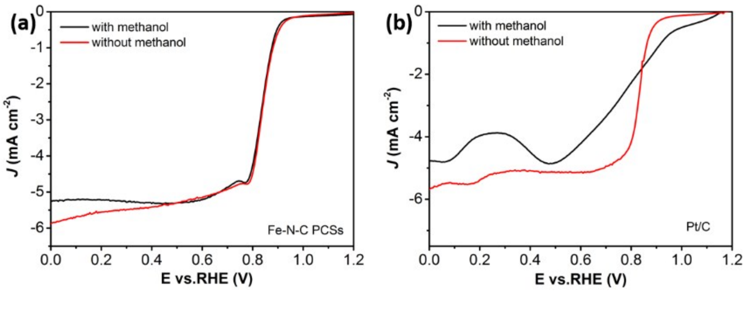

Fig. S25. LSV curves of the developed Fe-N-C PCSs (a), and commercial Pt/C catalyst (b) in the O_2-saturated 0.1 M KOH with the presence or absence of methanol, respectively.

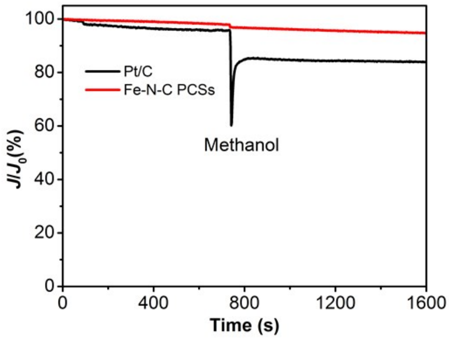

Fig. S26. The *i-t* measurements of Fe-N-C PCSs and Pt/C catalysts after the methanol injection in O_2-saturated 0.1 M KOH.

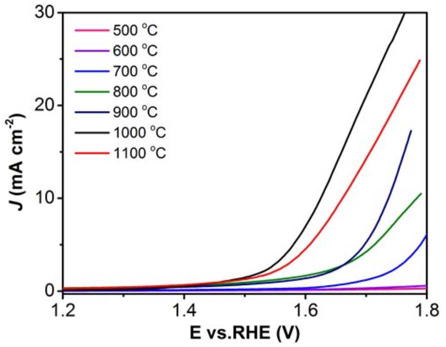

Fig. S27. LSV polarization curves of the series Fe-N-C PCSs catalysts obtained at different annealing temperature in 0.1 M KOH solution.

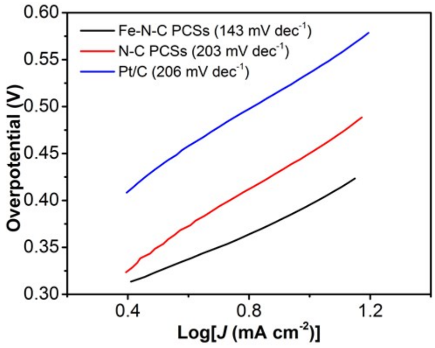

Fig. S28. Tafel plots of the developed catalysts and Pt/C catalyst in OER potential region.

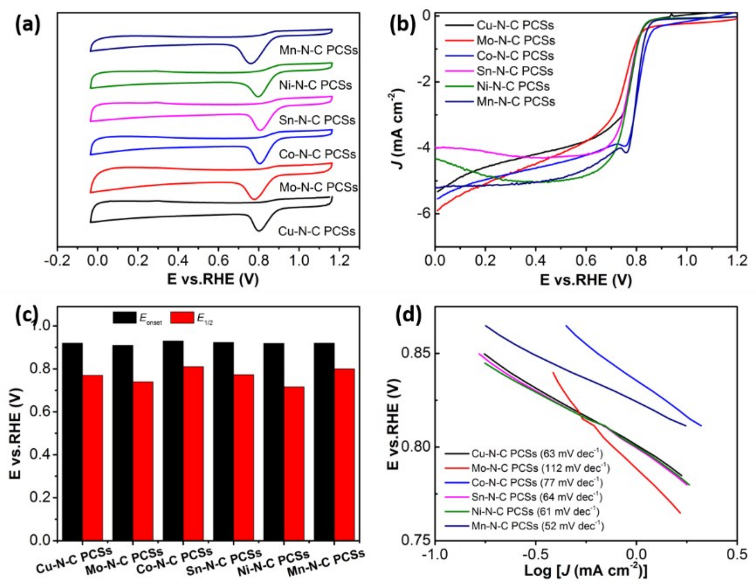

Fig. S29. (a) Cyclic voltammograms (CVs), (b) ORR polarization curves, (c) E_{onset} and $E_{1/2}$, (d) Tafel plots of the developed M-N-C PCSs catalysts. The CVs, LSV, and Tafel plots of the developed M-N-C PCSs catalysts exhibit the superior ORR performance with remarkable reaction kinetics.

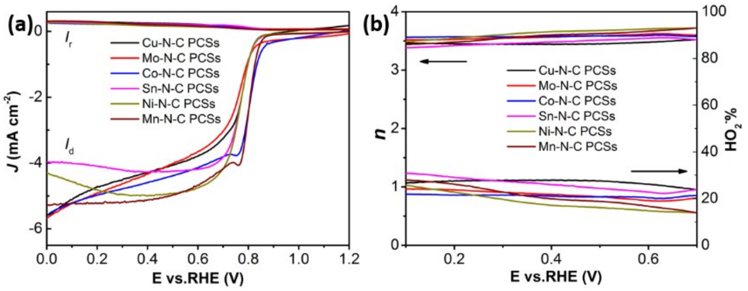

Fig. S30. (a) The disk current (I_d) and ring current (I_r) of the prepared M-N-C PCSs catalysts in the RRDE test. (b) HO_2^- yield and *n* determined by the RRDE curves of the developed catalysts. The RRDE analysis was performed to further investigate the ORR kinetics. The electron transfer numbers (n) of ORR on developed catalysts are around 3.8, associated with the low H_2O^-% yield, indicating four-electron pathways for ORR.

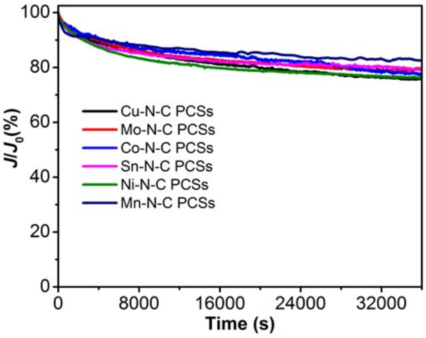

Fig. S31. Time dependence of ORR stability over M-N-C PCSs at 0.7 V (*vs.* RHE) in 0.1 M KOH media. Chronoamperometric response of the developed M-N-C PCSs exhibit a slight current decay for electrolysis over 36000 s, signifying that the composite catalysts are highly steady to withstand the activity degradation.

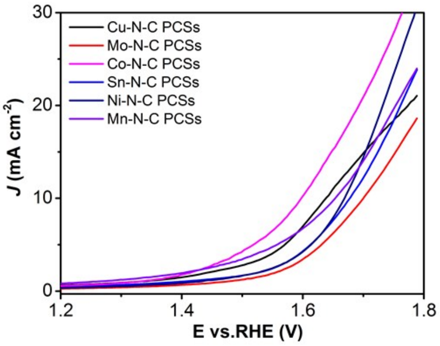

Fig. S32. OER polarization curve of the developed M-N-C PCSs catalysts in 0.1 M O_2-saturated KOH media. All the prepared M-N-C PCSs catalysts exhibits high OER activity. The difference on their LSV polarization curves may be attributed to the different metal active centers.

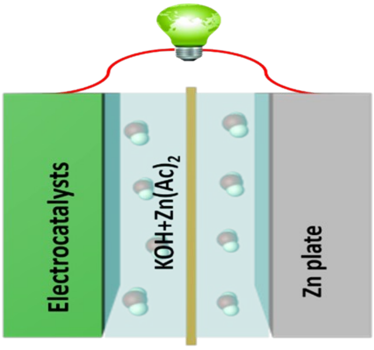

Fig. S33. Schematic illustration of the home-made rechargeable Zn-air battery.

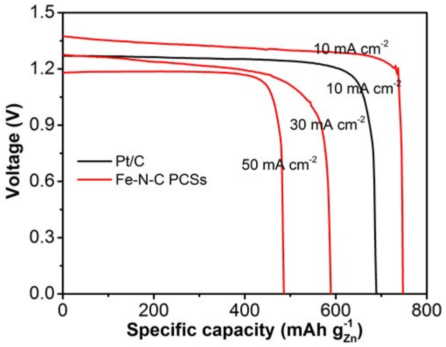

Fig. S34. Specific capacities of Zn-air batteries with the Fe-N-C PCSs, and Pt/C catalysts at different current densities.

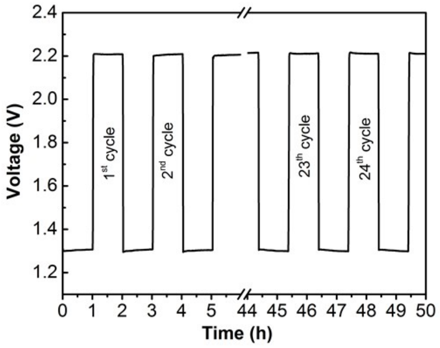

Fig. S35. Magnified observation of the galvanostatic charge/discharge cycling curves of Fe-N-C PCSs fabricated Zn-air battery in Fig. 5f.

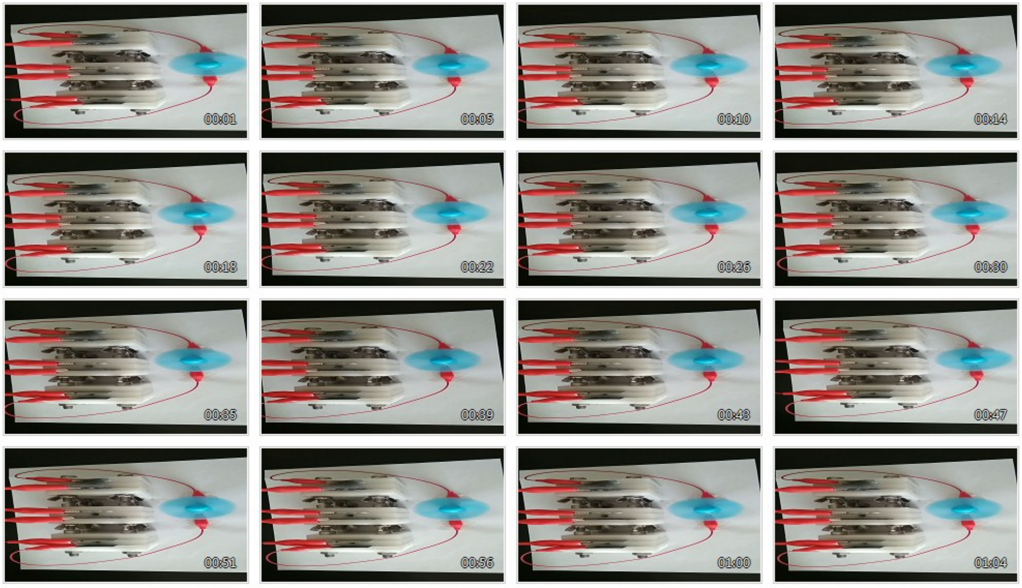

Fig. S36. Digital images of the mini fan driven by three Zn-air batteries assembled from Fe-N-C PCSs during different running times.

2. Supplementary tables

Table S1. Physicochemical properties and the electrochemical activities (0.1 M KOH) of the fabricated electrocatalysts.

Samples	**S_{BET} [a] ($\mathrm{m^2\ g^{-1}}$)**	**V_{total} [b] ($\mathrm{cm^3\ g^{-1}}$)**	**E_{onset} [c] (V)**	**$E_{1/2}$ [c] (V)**	**Tafel slope [c] ($\mathrm{mV\ dec^{-1}}$)**	**E_{onset} [d] (V)**	**$E_{\mathrm{j=10}}$ [d] (V)**	**Tafel slope [d] ($\mathrm{mV\ dec^{-1}}$)**	**E_{gap} [e] (V)**
500 °C [f]	29	0.04	0.80	0.56	-	-	-	-	-
600 °C [f]	36	0.07	0.80	0.59	-	-	-	-	-
700 °C [f]	74	0.15	0.82	0.62	-	1.70	-	-	-
800 °C [f]	110	0.19	0.87	0.67	-	1.59	1.78	-	-
900 °C [f]	151	0.43	0.91	0.76	-	1.59	1.74	-	-
Fe-N-C PCSs [f]	166	0.42	1.03	0.84	84	1.48	1.63	143	0.79
1100 °C [f]	129	0.37	0.94	0.82	-	1.48	1.66	-	-
Fe-N-C NC	16	0.02	0.80	-	-	1.76	-	-	-
N-C PCSs	178	0.45	0.96	0.77	111	1.49	1.68	203	0.91
N-C NC	21	0.03	0.78	-	-	1.76	-	-	-
Pt/C	-	-	1.01	0.83	85	1.50	1.77	206	0.94
Cu-N-C PCSs	163	0.41	0.92	0.77	63	-	1.64	-	0.87
Co-N-C PCSs	175	0.43	0.93	0.81	77	-	1.61	-	0.80
Ni-N-C PCSs	172	0.37	0.92	0.72	61	-	1.67	-	0.95
Sn-N-C PCSs	161	0.41	0.92	0.77	64	-	1.68	-	0.91
Mn-N-C PCSs	166	0.40	0.92	0.80	52	-	1.65	-	0.85
Mo-N-C PCSs	152	0.44	0.91	0.77	112	-	1.70	-	0.93

[a] The BET surface area, S_{BET}, was calculated using adsorption date in the relatively pressure range $P/P_0 = 0.05 - 0.30$.

[b] The total pore volume was calculated at the relatively pressure range $P/P_0 = 0.99$.

[c] These dates were measured in ORR potential range, and the potential at the current density of 0.1 mA $\mathrm{cm^{-2}}$ was defined as the onset potential (E_{onset}).

[d] These dates were measured in OER potential range, and the potential at the current density of 1.0 mA $\mathrm{cm^{-2}}$ was defined as the onset potential (E_{onset}).

[e] ΔE was the potential gap, and $\Delta E = E_{\mathrm{j=10}} - E_{1/2}$.

[f] These samples were the Fe-N-C PCSs obtained at different annealing temperature.

Table S2. Comparison of the electrocatalytic activity of recently reported bifunctional oxygen electrocatalysts in alkaline electrolyte.

Catalyst	**Loading mass of catalyst (mg cm^{-2})**	**$E_{1/2}$ (V)**	**$E_{j=10}$ (V)**	**E_{gap} (V)**	**Ref.**
Fe-N-C NCS	0.25	0.84	1.63	0.79	This work
Meso/micro-FeCoN$_x$-CN-30	0.100	0.886	1.67	0.784	[1]
N, P-doped carbon	0.15	0.85	1.85	~1.0	[2]
Co-N$_x$-C graphene	0.05	~0.800	1.75	0.95	[3]
$Fe_{0.5}Co_{0.5}O_x$/NrGO-300	0.50	-	1.487	0.74	[4]
GN-nanoribbon networks	0.600	0.840	1.66	0.820	[5]
Co@Co_3O_4/NC	0.210	0.80	1.65	0.850	[6]
Co_9S_8/NSPC8-45	0.249	0.74	1.57	0.83	[7]
Cu@NCNT/Co_xO_y	0.204	0.82	1.60	0.78	[8]
Co-N carbon nanocage	0.400	0.82	1.64	0.82	[9]
Egg-like carbon microsphere	0.136	0.69	~1.53	0.84	[10]
FeCo NPs doped carbon	0.200	0.92	1.73	0.81	[11]
NiCo/PFC aerogels	0.13	0.76	1.62	0.86	[12]
Fe@N-C	0.318	0.84	1.70	0.86	[13]
Fe-N-C	1.000	0.84	1.60	0.76	[14]
ZIF derived carbon frameworks	0.200	0.84	1.60	0.76	[15]
Nano-sized perovskite particles	0.639	0.66	1.60	0.94	[16]
$Co_xMn_{3-x}O_4$ carbon nanocomposites	0.18	0.68	1.78	1.10	[17]
$LaNi_{0.75}Fe_{0.25}O_3$/NC	0.051	0.670	1.68	1.010	[18]
$Ni_xCo_yO_4$/Co-NG	0.200	0.796	1.63	0.833	[19]
N-graphene/CNT	0.250	~0.70	1.63	0.930	[20]
CoO/N-doped graphene	0.714	0.81	1.57	0.76	[21]
Mn_xO_y/N-doped carbon	0.210	0.81	1.68	0.87	[22]
p-C_3N_4	~0.20	0.67	1.63	0.96	[23]
NiO/CoN Porous NW	0.200	0.68	1.53	~0.85	[24]
Ni_3Fe-N Doped Carbon	0.13	0.79	1.63	0.84	[25]
$Ni_xCo_yO_4$/Co–NG	0.2	0.796	1.629	0.833	[26]
Co–N/C 800	0.24	0.65	1.64	0.99	[27]

Table S3. The performance of reported liquid rechargeable Zn-air battery and our Zn-air battery.

Catalyst	Loading mass (mg cm^{-2})	Voltage @ 10 mA cm^{-2}	Peak power density (mW cm^{-2})	Energy density (Wh kg^{-1})	Cycling conditions and stability	Ref.
Fe-N-C PCSs	1.0	1.34	108	-	10 mA cm^{-2}, 20 min/cycle for 300 cycles; no obvious voltage decay	This work
NCN-1000-80	2.0	1.21	207	806	10 mA cm^{-2}, 20 min/cycle for 1000 cycles; no obvious voltage decay	[28]
N-CN9	1.0	1.10	41	-	10 mA cm^{-2}, 10 min/cycle for 30 cycles; voltage gap increased ~0.33 V	[29]
NCNF-1000	2.0	1.20	185	-	10 mA cm^{-2}, 10 min/cycle for 500 cycles; voltage gap increased ~0.13 V	[30]
3D-CNTA	2.0	1.31	157	-	10 mA cm^{-2}, 10 min/cycle for 240 cycles; voltage gap increased ~0.14 V	[31]
1100-CNS	2.0	1.25	151	-	10 mA cm^{-2}, 11 min/cycle for 300 cycles; voltage gap increased ~0.08 V	[32]
PS-CNS	/	1.25	231	785	2 mA cm^{-2}, 12 min/cycle for 600 cycles; no obvious voltage decay	[33]
Co/CoO@Co-N-C	2.0	1.25	157	-	10 mA cm^{-2}, 10 min/cycle for 100 cycles; voltage gap increased ~0.19 V	[34]
NiO/CoN PINWs	/	0.19	80	836	3 mA cm^{-2}, 10 min/cycle for 50 cycles; voltage gap increased ~0.25 V	[35]
Ni_3Fe/N-C	2.0	1.20	/	634	10 mA cm^{-2}, 4 h/cycle for 105 cycles; voltage gap increased ~0.20 V	[36]
N-GCNT/FeCo-3	2.0	1.26	89	653	20 mA cm^{-2}, 20 min/cycle for 27 cycles; voltage gap increased ~0.03 V	[37]
CoZn-NC-700	1.2	1.22	152	694	10 mA cm^{-2}, 10 min/cycle for 385 cycles; voltage gap increased ~0.37 V	[38]
MnO@Co-N/C	0.6	1.18	130.3	-	5, 20 min per cycle for 1900 Cycles (633 h)	[39]
Co_3O_4/N-rGO	-	-	-	-	3, 20 min per cycle for 75 cycles (25 h)	[40]
$Fe_{0.5}Co_{0.5}O_x$/NrGO	1.0	1.19	86	904	10, 2 h per cycle for 60 cycles (120 h)	[41]

$Co_3FeS_{1.5}(OH)_6$	0.5	1.16 (20 mA cm^{-2})	113.1	-	2, 20 min per cycle for 108 cycles (36 h)	[42]
Co_3O_4/N-CNTAs	2.0	1.15 (5 mA cm^{-2})		734	5, 10 min per cycle for100 cycles (16.7 h)	[43]
Co-N_x-C	0.50	1.12 (20 mA cm^{-2})	152	840	2, 20 min per cycle for 180 cycles (60 h)	[3]
CoS_x@PCN/rGO	2.0	-	-	-	10, 6.6 min per cycle for 394 cycles (43.8 h)	[44]
NPMC-1000	0.5	1.26 (5 mA cm^{-2})	55	835	2, 10 min per cycle for 180 cycles (30 h)	[45]
RuO_2-coated MCNAs	1.5~2.0	1.25 (4 mA cm^{-2})	-	-	4, 20 min per cycle for 100 cycles (34 h)	[46]
C-MOF-C2-900	0.5	1.28 (2 mA cm^{-2})	105	-	10, 20 min per cycle for 90 cycles (30 h)	[47]
S-GNS/$NiCo_2S_4$	-	1.19	216.3	-	10, 40 min per cycle for 150 cycles (100 h)	[48]

3. Supplementary references

[1] S. Li, C. Cheng, X. Zhao, J. Schmidt, A. Thomas, *Angew. Chem. Int. Ed.* **2018**, 57, 1856.

[2] J. Zhang, Z. Zhao, Z. Xia, L. Dai, *Nature Nanotech.* **2015**, 10, 444.

[3] C. Tang, B. Wang, H. F. Wang, Q. Zhang, *Adv. Mater.* **2017**, 29, 1703185.

[4] L. Wei, H. E. Karahan, S. Zhai, H. Liu, X. Chen, Z. Zhou, Y. Lei, Z. Liu, Y. Chen, *Adv. Mater.* **2017**, 29, 1701410.

[5] H. B. Yang, J. Miao, S.-F. Hung, J. Chen, H. B. Tao, X. Wang, L. Zhang, R. Chen, J. Gao, H. M. Chen, *Science advances* **2016**, 2, e1501122.

[6] A. Aijaz, J. Masa, C. Rösler, W. Xia, P. Weide, A. J. Botz, R. A. Fischer, W. Schuhmann, M. Muhler, *Angew. Chem. Int. Ed.* **2016**, 55, 4087.

[7] H.-x. Zhong, K. Li, Q. Zhang, J. Wang, F.-l. Meng, Z.-j. Wu, J.-m. Yan, X.-b. Zhang, *NPG Asia Materials* **2016**, 8, e308.

[8] X. Zhao, F. Li, R. Wang, J. M. Seo, H. J. Choi, S. M. Jung, J. Mahmood, I. Y. Jeon, J. B. Baek, *Adv. Funct. Mater.* **2017**, 27, 1605717.

[9] S. Liu, Z. Wang, S. Zhou, F. Yu, M. Yu, C. Y. Chiang, W. Zhou, J. Zhao, J. Qiu, *Adv. Mater.* **2017**, 29, 1700874.

[10] H. Wu, J. Geng, H. Ge, Z. Guo, Y. Wang, G. Zheng, *Adv. Energy Mater.* **2016**, 6, 1600794.

[11] C. Y. Su, H. Cheng, W. Li, Z. Q. Liu, N. Li, Z. Hou, F. Q. Bai, H. X. Zhang, T. Y. Ma, *Adv. Energy Mater.* **2017**, 7, 1602420.

[12] G. Fu, Y. Chen, Z. Cui, Y. Li, W. Zhou, S. Xin, Y. Tang, J. B. Goodenough, *Nano Lett.* **2016**, 16, 6516.

[13] J. Wang, H. Wu, D. Gao, S. Miao, G. Wang, X. Bao, *Nano Energy* **2015**, 13, 387.

[14] M. Lefèvre, E. Proietti, F. Jaouen, J.-P. Dodelet, *Science* **2009**, 324, 71.

[15] B. Y. Xia, Y. Yan, N. Li, H. B. Wu, X. W. D. Lou, X. Wang, *Nature Energy* **2016**, 1, 15006.

[16] X.-Y. Yu, Y. Feng, B. Guan, X. W. D. Lou, U. Paik, *Energy Environ. Sci.* **2016**, 9, 1246.

[17] C. Li, X. Han, F. Cheng, Y. Hu, C. Chen, J. Chen, *Nature Commun.* **2015**, 6, 7345.

[18] W. G. Hardin, J. T. Mefford, D. A. Slanac, B. B. Patel, X. Wang, S. Dai, X. Zhao, R. S. Ruoff, K. P. Johnston, K. J. Stevenson, *Chem. Mater.* **2014**, 26, 3368.

[19] Y. Hao, Y. Xu, J. Liu, X. Sun, *J. Mater. Chem. A* **2017**, 5, 5594.

[20] G. L. Tian, M. Q. Zhao, D. Yu, X. Y. Kong, J. Q. Huang, Q. Zhang, F. Wei, *Small* **2014**, 10, 2251.

[21] S. Mao, Z. Wen, T. Huang, Y. Hou, J. Chen, *Energy Environ. Sci.* **2014**, 7, 609.

[22] J. Masa, W. Xia, I. Sinev, A. Zhao, Z. Sun, S. Grützke, P. Weide, M. Muhler, W. Schuhmann, *Angew. Chem. Int. Ed.* **2014**, 53, 8508.

[23] T. Y. Ma, J. Ran, S. Dai, M. Jaroniec, S. Z. Qiao, *Angew. Chem. Int. Ed.* **2015**, 54, 4646.

[24] J. Yin, Y. Li, F. Lv, Q. Fan, Y.-Q. Zhao, Q. Zhang, W. Wang, F. Cheng, P. Xi, S. Guo, *ACS Nano* **2017**, 11, 2275.

[25] G. Fu, Z. Cui, Y. Chen, Y. Li, Y. Tang, J. B. Goodenough, *Adv. Energy Mater.* **2017**, 7, 1601172.

[26] Y. Hao, Y. Xu, J. Liu, X. Sun, *J. Mater. Chem. A* **2017**, 5, 5594.

[27] W. Hu, Q. Wang, S. Wu, Y. Huang, *J. Mater. Chem. A* **2016**, 4, 16920.

[28] H. Jiang, J. Gu, X. Zheng, M. Liu, X. Qiu, L. Wang, W. Li, Z. Chen, X. Ji, J. Li, *Energy Environ. Sci.* **2019**, 12, 322.

[29] C. Zhang, G. Zhang, H. Li, Y. Chang, Z. Chang, J. Liu, X. Sun, *Electrochim. Acta* **2017**, 247, 1044.

[30] Q. Liu, Y. Wang, L. Dai, J. Yao, *Adv. Mater.* **2016**, 28, 3000.
[31] S. Wang, J. Qin, T. Meng, M. Cao, *Nano Energy* **2017**, 39, 626.
[32] Z. X. Pei, H. F. Li, Y. Huang, Q. Xue, Y. Huang, M. S. Zhu, Z. F. Wang, C. Y. Zhi, *Energy Environ. Sci.* **2017**, 10, 742.
[33] S. S. Shinde, C. H. Lee, A. Sami, D. H. Kim, S. U. Lee, J. H. Lee, *ACS Nano* **2017**, 11, 347.
[34] X. Zhang, R. Liu, Y. Zang, G. Liu, G. Wang, Y. Zhang, H. Zhang, H. Zhao, *Chem. Commun.* **2016**, 52, 5946.
[35] J. Yin, Y. Li, F. Lv, Q. Fan, Y. Q. Zhao, Q. Zhang, W. Wang, F. Cheng, P. Xi, S. Guo, *ACS Nano* **2017**, 11, 2275.
[36] G. Fu, Z. Cui, Y. Chen, Y. Li, Y. Tang, J. B. Goodenough, *Adv. Energy Mater.* **2016**, 7, 1601172.
[37] C.-Y. Su, H. Cheng, W. Li, Z.-Q. Liu, N. Li, Z. Hou, F.-Q. Bai, H.-X. Zhang, T.-Y. Ma, *Adv. Energy Mater.* **2017**, 7, 1602420.
[38] X. Wu, X. Han, X. Ma, W. Zhang, Y. Deng, C. Zhong, W. Hu, *ACS Appl. Mater. Interfaces* **2017**, 9, 12574.
[39] Y. Chen, Y. Guo, H. Cui, Z. Xie, X. Zhang, J. Wei, Z. Zhou, *J. Mater. Chem. A* **2018**, 6, 9716.
[40] Y. Li, C. Zhong, J. Liu, X. Zeng, S. Qu, X. Han, Y. Deng, W. Hu, J. Lu, *Adv. Mater.* **2018**, 30, 1703657.
[41] L. Wei, H. E. Karahan, S. Zhai, H. Liu, X. Chen, Z. Zhou, Y. Lei, Z. Liu, Y. Chen, *Adv. Mater.* **2017**, 29, 1701410.
[42] H. F. Wang, C. Tang, B. Wang, B. Q. Li, Q. Zhang, *Adv. Mater.* **2017**, 29, 1702327.
[43] W. Tian, H. Li, B. Qin, Y. Xu, Y. Hao, Y. Li, G. Zhang, J. Liu, X. Sun, X. Duan, *J. Mater. Chem. A* **2017**, 5, 7103.
[44] W. Niu, Z. Li, K. Marcus, L. Zhou, Y. Li, R. Ye, K. Liang, Y. Yang, *Adv. Energy Mater.* **2018**, 8, 1701642.
[45] J. Zhang, Z. Zhao, Z. Xia, L. Dai, *Nature Nanotech.* **2015**, 10, 444.
[46] Z. Guo, C. Li, W. Li, H. Guo, X. Su, P. He, Y. Wang, Y. Xia, *J. Mater. Chem. A* **2016**, 4, 6282.
[47] M. Zhang, Q. Dai, H. Zheng, M. Chen, L. Dai, *Adv. Mater.* **2018**, 30, 1705431.
[48] W. Liu, J. Zhang, Z. Bai, G. Jiang, M. Li, K. Feng, L. Yang, Y. Ding, T. Yu, Z. Chen, *Adv. Funct. Mater.* **2018**, 28, 1706675.